10-16-2023

Impact of Thermal Maturation of the Upper Cretaceous Bituminous Limestone of Attarat Um Ghudran Central Jordan on Calcareous Nannofossil Preservation

Mohammad Alqudah
Yarmouk University

Mohammad Al Alaween
Yarmouk University; Zayed University

Adam Fermor
Applied Petroleum Technology (U.K.)

Ezaldeen Ali
Ministry of Energy and Mineral Resources, Amman, 11814, Jordan

Thomas Wagner
Heriot-Watt University

See next page for additional authors

ACS OMEGA

Open Access

http://pubs.acs.org/journal/acsodf

Article

Impact of Thermal Maturation of the Upper Cretaceous Bituminous Limestone of Attarat Um Ghudran Central Jordan on Calcareous Nannofossil Preservation

Mohammad Alqudah, Mohammad Al Alaween, Adam Fermor, Ezaldeen Ali, Thomas Wagner, Mohammed Hail Alhakimi,* and Afikah Rahim

Cite This: *ACS Omega* 2023, 8, 39830−39846

Read Online

ACCESS | Metrics & More | Article Recommendations

ABSTRACT: Oil shale deposits of the Late Cretaceous from three boreholes in central Jordan were examined to assess the impact of thermal maturation on the content of nannofossils. Thermal activity has been shown to have a strong effect on organic matter content and composition but its effect on calcareous nannofossil assemblages remains inconclusive. This study aims to determine the impact of thermal maturation on nannofossil assemblages and to compare this to an estimated maturity level based on bulk geochemical analysis. Micropaleontological and geochemical analyses were conducted on 31 samples from three oil shale wells drilled in Attarat Um Ghudran central Jordan. Several types of nannofossil preservation have been recorded, including dissolution, overgrowth, and breakage. In the Jordan oil shale sections, nannofossils exhibit a variety of preservation types, with intense dissolution in the middle part of the study sections. The vast majority of the samples had high TOC enrichment, with 29 samples exceeding values of >10%. Kerogen recovery and quality from the oil shale are very good, with a predominance of fluorescent amorphous organic matter (AOM) and minor algal components. The low fluorescence preservation index (FPI), which is 1 in most of the samples, indicates that alteration occurred due to intense thermal activities in the study interval. The palynomorph and AOM fluorescence, ranging from a spore coloration index (SCI) of 3 to 5, suggest that the studied samples were approaching the oil window. A correlation between the nannofossil preservation and geochemical parameters shows a predominance of poorly preserved nannofossils along with high total organic carbon contents and an elevated hydrogen index (HI). We show that low FPI values and a higher level of maturity are associated with poor nannofossil preservation, suggesting that nannofossils, in conjunction with petrographic analysis of kerogen, could be used as a rapid screening technique for estimating levels of oil-shale maturity. The nature of the tectonism in the study area, including faulting and a metamorphosed zone, enhanced the maturity, which might explain why the nannofossils were so significantly affected.

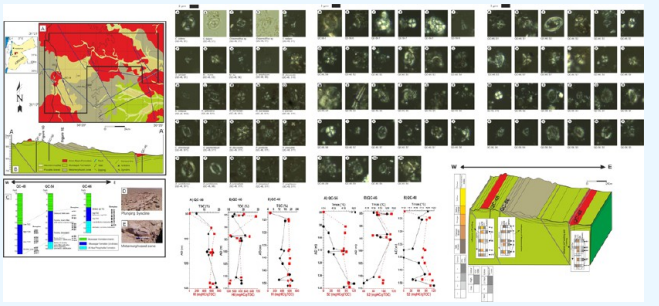

1. INTRODUCTION

Organic-rich sedimentary rocks of the Late Cretaceous in Jordan are composed of inorganic and organic components. Black shale/marl layers are characterized by high total organic carbon (TOC), elemental C/N, and Rock-Eval hydrogen index values. Increments in these measurements are considered to be indications of the production of marine organic matter. These organic productions can be associated with inorganic carbon productivity in organisms like coccolithophores, which on the one hand produce organic matter and on the other hand produce carbonates as a shield. TOC concentrations, in such cases, decrease as sedimentation rates increase, reflecting dilution of the organic matter.[1,2] Many authors have assessed the rate of R-mode coccolithophore growth to estimate the primary productivity and correlate high rates with high TOC and HI values.[3,4] Traditionally, organic components are subjected to maturity assessments.

Determining the maturity level of the organic matter (OM) during certain phases of exploration is critical, and various geochemical techniques, such as pyrolysis analysis,[5−7] vitrinite reflectance,[8−10] and gas chromatography,[11,12] have been used to understand this for years. Each has its advantages and drawbacks.

However, maturity assessment is not straightforward and has limitations,[13] bearing in mind possible effects of mud additives and lubricants,[6,14] mineral matrix effects on pyrolysate, and the

Received: August 15, 2023
Accepted: September 29, 2023
Published: October 16, 2023

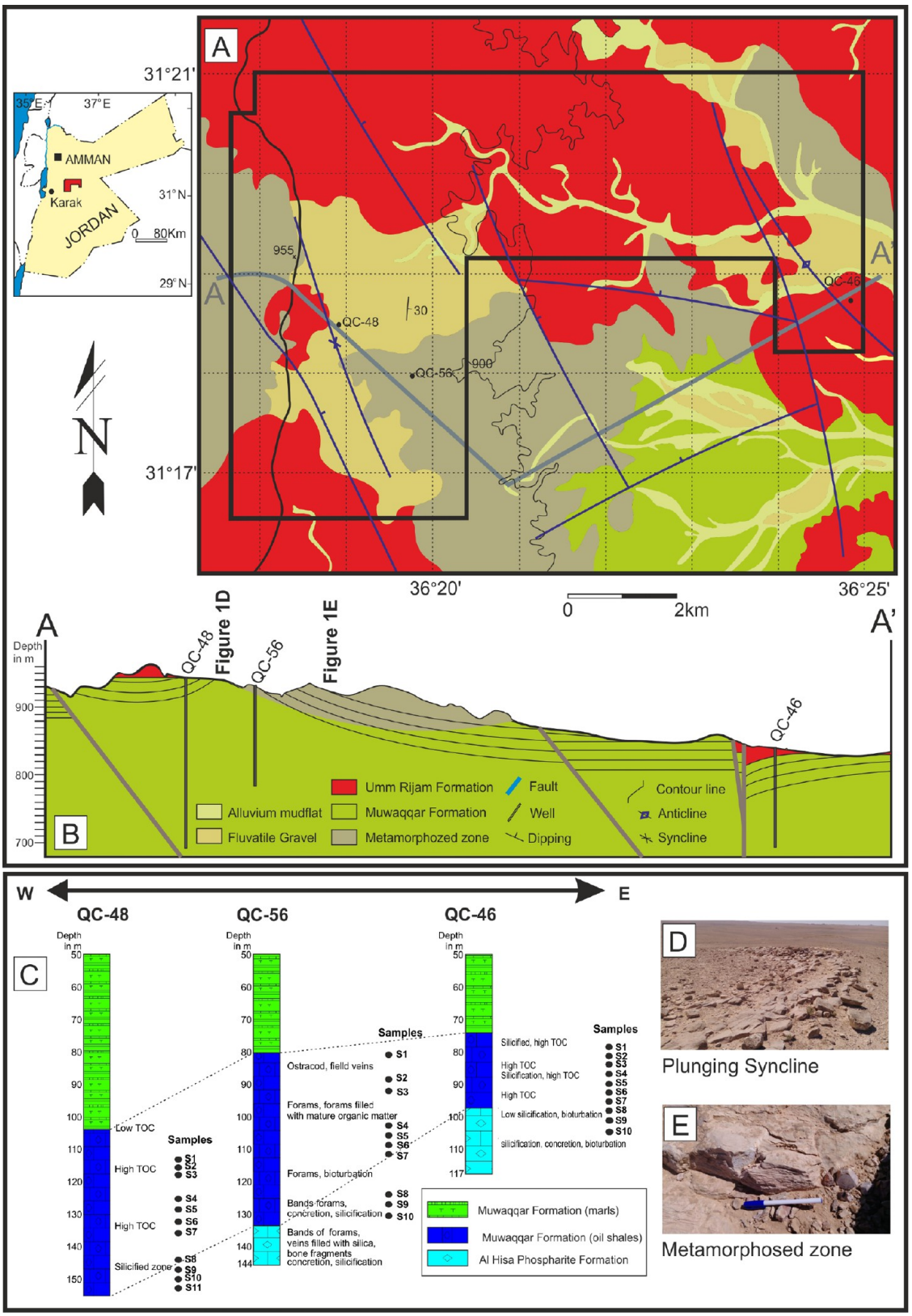

Figure 1. (A) Map (Modified after[32]) and (B) cross section illustrating the geology of the study area. (C) Lithological correlation of Boreholes QC-48, QC-56, and QC-46. Images showing illustrations of (D) a plunging syncline and (E) the metamorphosed zone. Field photographs were taken by Mohammad Alqudah.

production of pyrolysis.[15] As for the pyrolysis parameter T_{max}, a proxy indicator of thermal stress, the assessment of optical thermal maturity can be affected by various factors, including the preservation of kerogen, a lack of terrestrial components, and the suppression of vitrinite reflectivity in oil-prone source rocks. Additionally, any organic drilling additives will be

https://doi.org/10.1021/acsomega.3c06033
ACS Omega 2023, 8, 39830−39846

present in the kerogen isolate. Although these are usually distinguished from *in situ* particles by their immaturity, the sheer volume of contaminant particles can occasionally obscure native components, making kerogen-typing and maturity assessment challenging.

A number of recent studies have identified thermal stress signatures in a wide range of fossil groups, such as dinoflagellates, nannofossils, bivalves, echinoids, and sponges.[16−18] Sponge spicules, for example, were found to have been melted by the Miocene Ewing impact in the abyssal equatorial Pacific Ocean.[16]

Palynomorphs are highly sensitive to thermal stressors, including the depth of burial or contact metamorphism, and OM trapped in the mineralized skeletal components of microfossils undergoes a series of chemical and physical alterations that lead to color transformations.[20] The composition and preservation of nannofossils also respond to weathering, reworking, oxidation, and thermal metamorphism[20] and, once calibrated to other maturity proxies, have the potential to facilitate assessment of the level of thermal maturation with limited analytical efforts.

A correlation between nannofossil preservation and geochemical parameters including Rock-Eval and organic petrography represented by the fluorescence preservation index (FPI) could be a new and useful rapid screening technique for estimating levels of oil shale maturity.

The purpose of this study is to determine the impact of thermal maturation on nannofossil assemblages and to compare this to an estimated maturity level based on bulk geochemical analysis, with the expectation that the nannofossil assemblages would serve as a biothermometer for the maturation of OM in the Upper Cretaceous oil-shale successions in Jordan.

2. GEOLOGICAL SETTING

In the Maastrichtian, Jordan was situated at the southern margin of the Neo-Tethys Ocean where deep-water, locally organic-rich chalk−marl deposition was taking place on the epicontinental platform.[21−23] A rapid eustatic sea-level rise during this time resulted in widespread marine on lap over an extensive area of the Arabian Plate.[24] The chalk−marl and organic-rich marls deposited range from Late Coniacian to Late Eocene in age and span the Cretaceous−Palaeogene boundary, which is marked by a depositional hiatus in the upper part of the Muwaqqar Chalk−Marl (MCM) Formation.[25,26] The Syrian Arc fold system affected the Levant intensively in the Late Cretaceous, coinciding with the closure of the Neo-Tethys.[27] This system influenced sediment accumulation in the grabens, resulting in the deposition of organic-rich sediments in the basins.[28−30] The organic-rich sediments that accumulated in the mosaic of basins during the Late Cretaceous vary in thickness over short distances, with the thickest sequences located near the basin centers, indicating intensive tectonic effects during their deposition[31] (Figure 1). One economically important basin is the Lajun Basin in central Jordan, which extends from Lajun in the west to Attarat Um Ghudran in the east. This basin is bounded by normal faults, with the number of faults increasing on the western side of the study area (Attarat Um Ghudran), whereas folding is the more prevalent structural feature in the eastern part.

The beds, as revealed by a structural evaluation of the Attarat Um Ghudran location, dip at 2−5° NE and are dominated by straight and slightly curved faults and lineaments[32] (Figure 1A). The study area was intersected by a network of numerous faults, mostly NW−SE trending, accompanied by different behaviors and displacements[33] (Figure 1B). The dominant structures include the E−W-trending Siwaqa Fault, Zarqa Ma'in strike−slip faults, the NW−SE Sirhan Fault System and the Karak Fayha Fault, along with associated structural features, such as horsts, grabens, folds, and tilted blocks.[34] Folding was present in the study area, where a plunging syncline was discovered during our fieldwork (Figure 1D).

The Muwaqqar Chalk Marl (MCM) Formation is the main lithological unit exposed in the study area. This formation comprises shallow to deep marine sediments deposited during the Maastrichtian.[35,36] It includes thick-bedded chalky marl, bituminous marl, marly limestone, and chalk and is overlain unconformably by the Umm Rijam Chert (URC) Limestone Formation[36] (Figure 1). The bituminous marl of the MCM Formation partially accumulated in anoxic basins in the deepest parts of the grabens.[31,36−38] The URC Formation has been divided into two parts − the lower part is ∼20−40 m-thick, consists of chalky limestone, and contains varicolored marbles (i.e., it has been metamorphosed)[39] (Figure 1). It has been suggested that these marbles formed at high temperatures in tandem with the thermal combustion of OM in an alteration-restricted zone.[35,40] The upper part of the formation consists of alternating limestone and chert beds overlain by chalk and concretions of microcrystalline limestone.[37]

3. MATERIALS AND METHODS

3.1. Samples and Sampling Procedure. The three cores investigated in this study came from an explorative program that drilled a total of 52 boreholes and covered 64.3 km^2 of the concession area in central Jordan. The aim of the drilling was to evaluate the potential of the oil-shale strata in the region. Three of the boreholes − QC-46, QC-48, and QC-56 − contained continuous organic-rich chalky-marly limestone (i.e., oil shale) layers with thicknesses of 53, 51, and 44 m, and overburdens of 79, 103, and 61 m, respectively. In total, 31 visually homogeneous samples (in terms of color, lithology, and bioturbation index), covering the Late Cretaceous (Maastrichtian) to Cenozoic (Eocene), were selected and crushed (Figure 1).

3.2. Nannofossil Preparation and Analysis. Smear-slides were prepared for determining the nannofossil assemblages and their preservation following the standard method of Burnett 1998. The slides were examined under a polarizing light microscope at 1500× magnification in the Earth and Environmental Sciences Department of Yarmouk University (Jordan). The nannofossil biozonation schemes of Perch-Nielsen[41] and Burnett et al.[42] were applied to interpret the Maastrichtian biostratigraphy, with Martini[43] being used for the Palaeogene biozones. The nannofossil preservation scale of Roth[44] was applied in order to record the preservation of the nannofossil assemblages on each slide. In this scheme, D is dissolution, with '1' referring to a low dissolution effect, E is etching, with '1' referring to low etching in the sample, O is overgrowth, with '1' referring to low overgrowth in the sample, and B is broken, with '1' referring to a low proportion of broken species. The nannofossil abundances were defined as follows: abundant (A) is more than 10 specimens per field of view (FOV); common (C) is 1−10 specimens per FOV; few (F) is 1 specimen per 2−50 FOVs; rare (R) is 1 specimen per

https://doi.org/10.1021/acsomega.3c06033
ACS Omega 2023, 8, 39830−39846

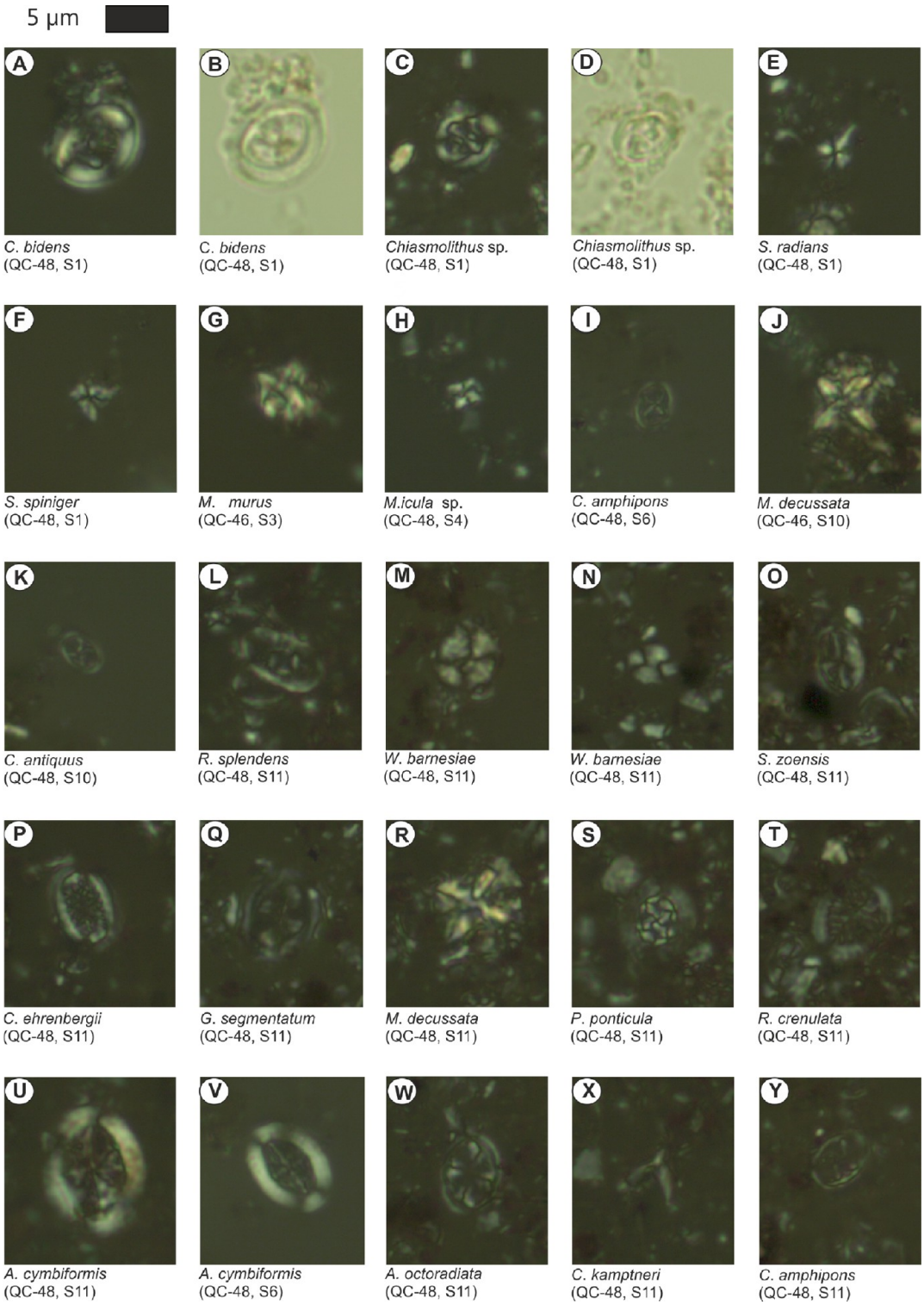

Figure 2. Illustration of moderately well-preserved nannofossils from boreholes QC-46 and QC-48. (A) *C. bidens*, under a cross polarizer (XPL); (B) *C. bidens* under plane polarizer (PPL); (C) *Chiasmolithus* sp., XPL; (D) *Chiasmolithus* sp., PPL; (E) *S. radians*, XPL; (F) *S. spiniger*, XPL; (G, H) *Micula* spp., XPL; (I) *C. amphipons*, XPL; (J) *M. decussata*, XPL; (K) *C. antiquus*, XPL; (L) *R. splendens*, XPL; (M, N) *W. barnesiae*, XPL; (O) *S. zoensis*, XPL; (P) *C. ehrenbergii*, XPL; (Q) *G. segmentatum*, XPL; (R) *M. decussata*, XPL; (S) *P. ponticula*, XPL; (T) *R. crenulata*, XPL; (U, V) *A. cymbiformis*, XPL; (W) *A. octoradiata*, XPL; (X) *C. kamptneri*, XPL; (Y) *C. amphipons* (XPL).

51−100 FOVs; and absent (NO) is no specimens in more than 100 FOVs.

3.3. Bulk Geochemical Analysis. The total organic carbon (TOC) contents of 31 air-dried, crushed, and homogenized samples from the three cores were determined using a Leco SC-632 instrument following the prior removal of the carbonate by hydrochloric acid (HCl) treatment. Svalbard rock was used as the geochemical standard, which was run after every ninth sample and compared to the acceptable range given in the Norwegian Industry Guide. Rock pyrolysis

https://doi.org/10.1021/acsomega.3c06033
ACS Omega 2023, 8, 39830−39846

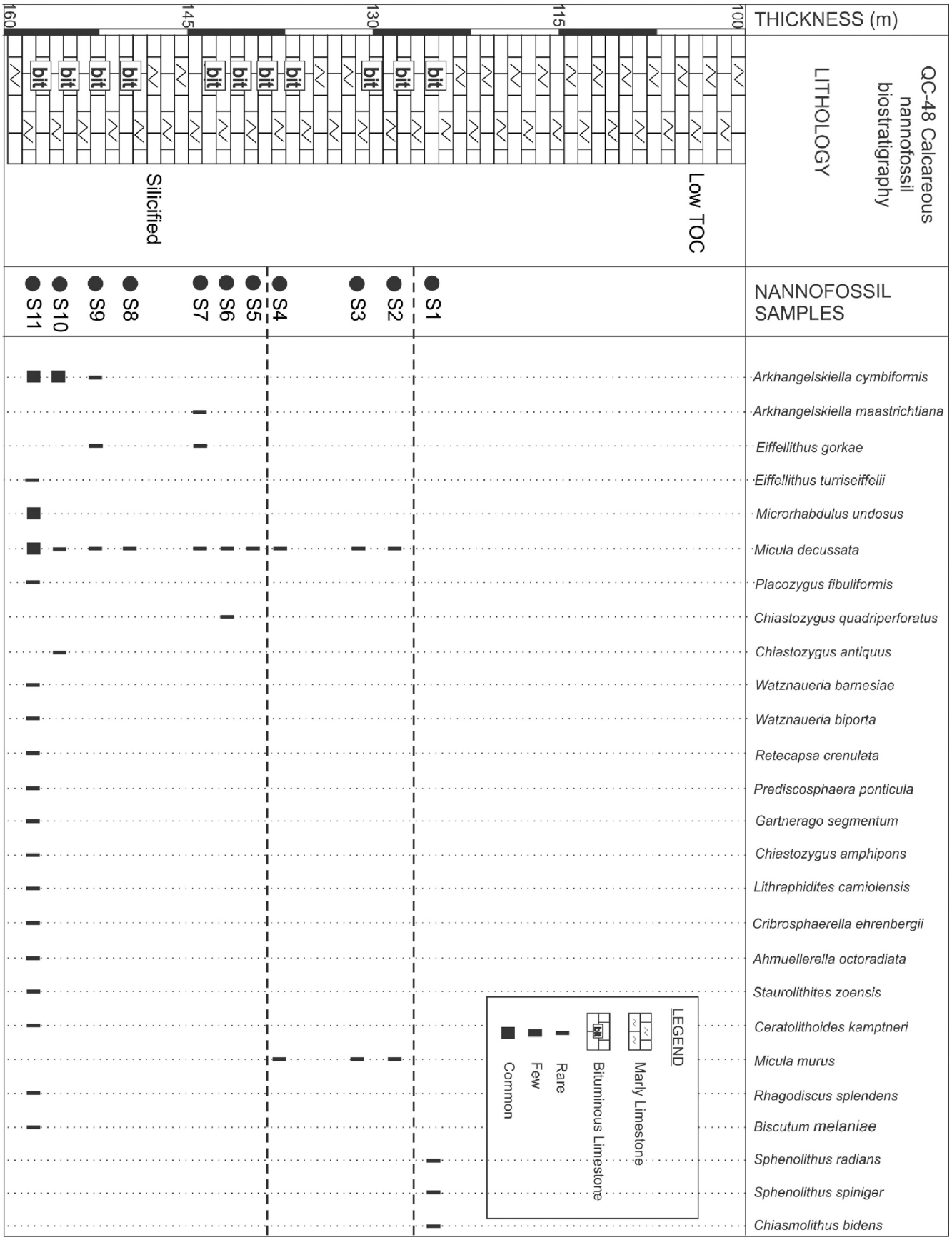

Figure 3. Nannofossil distribution chart, borehole QC-48.

https://doi.org/10.1021/acsomega.3c06033
ACS Omega 2023, 8, 39830−39846

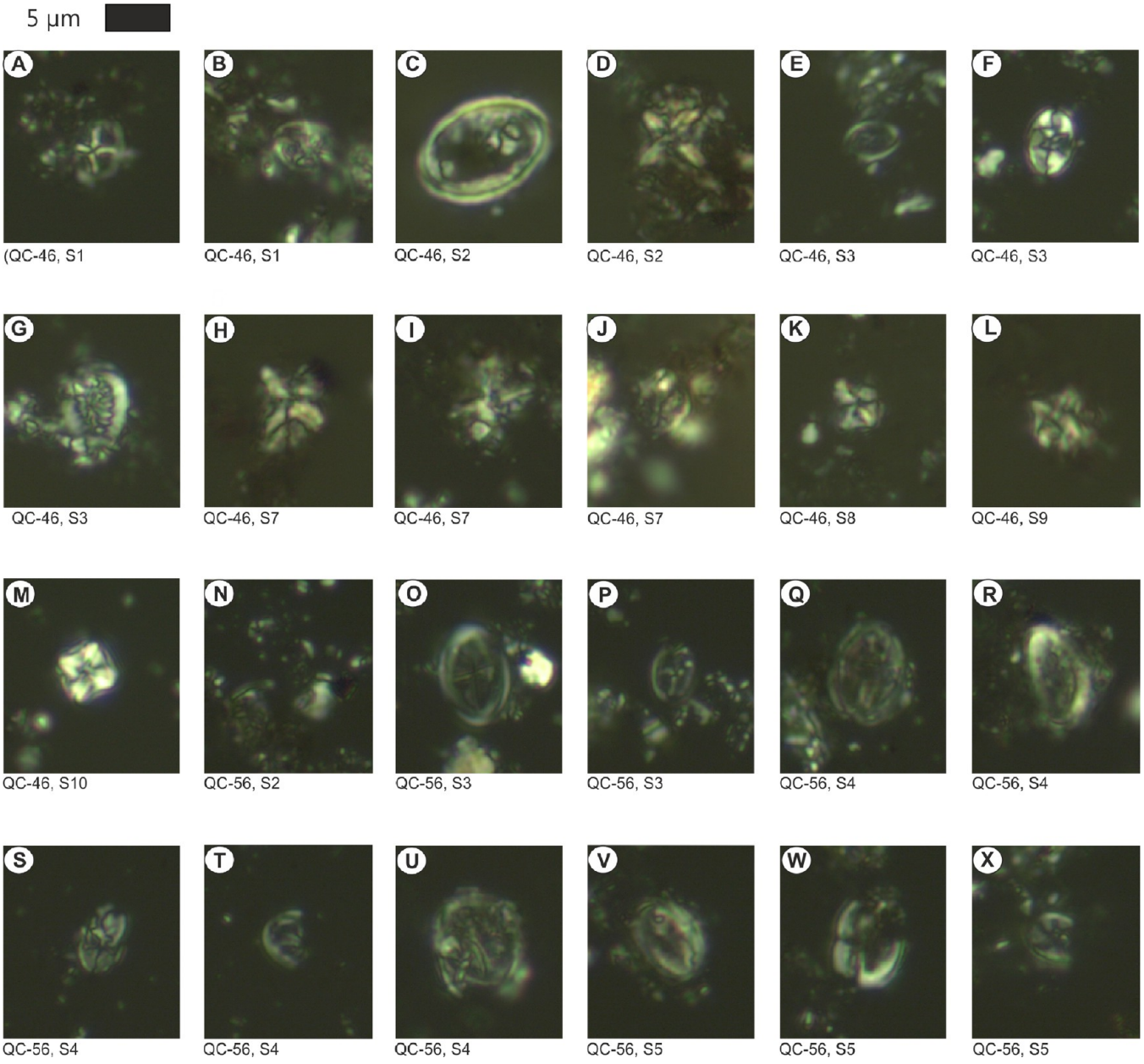

Figure 4. Effect of rock thermal maturation on nannofossil specimens in boreholes QC-46 and QC-56. (A–X) Microphotographs of deformed species.

analyses, using ∼100 mg finely ground aliquots of air-dried sample, were performed using a Rock-Eval 6 analyzer with a flame ionization detector for two stages of the pyrolysis temperature program (300 °C for ∼3 min, increasing by 25 °C/min to 650 °C, and maintained for 3 min). The S1, S2, and S3 data obtained from the analyses were in mg/g. The hydrogen index (HI: mg HC/g TOC), oxygen index (OI: mg carbon dioxide [CO_2]/g TOC), production index (PP: mg/g), and production index (PI) were then calculated from these Rock-Eval results.

3.4. Microscopic Examinations. Kerogen and palynomorph coloration and fluorescence analyses were conducted in transmitted white light using a Zeiss Axioplan microscope fitted with Zeiss Epiplan Neofluar objectives (10, 40, and 63×) and 10× eyepieces located at APT company, Aberdeen. The ultraviolet (UV) fluorescence colors were observed in reflected short-wavelength blue light using an excitation filter passing light with a 365 nm wavelength, a barrier filter with a 397 nm wavelength, and a dichromatic beam splitter with a 395 nm wavelength. The slides used for the spore coloration work were prepared using standard palynological techniques[20] (HCl and hydrofluoric acid [HF]), but omitting the oxidative stages.

The spore colors were determined using a > 10 μm fraction, whereas the kerogen was described using the total kerogen. The spore-color and kerogen-typing analyses were supplemented by observations of exinite and kerogen fluorescence under reflected blue light excitation.

In order to ascertain the suitability of the different methods available, kerogen isolates from three QC-56 samples (2, 5, and 9) were screened in transmitted and reflected light to determine the presence of the organic constituents used in the assessment of the thermal maturity of sediments. This initial screening showed that the kerogens in all of the samples were predominantly fluorescent AOM with fairly abundant

https://doi.org/10.1021/acsomega.3c06033
ACS Omega 2023, 8, 39830−39846

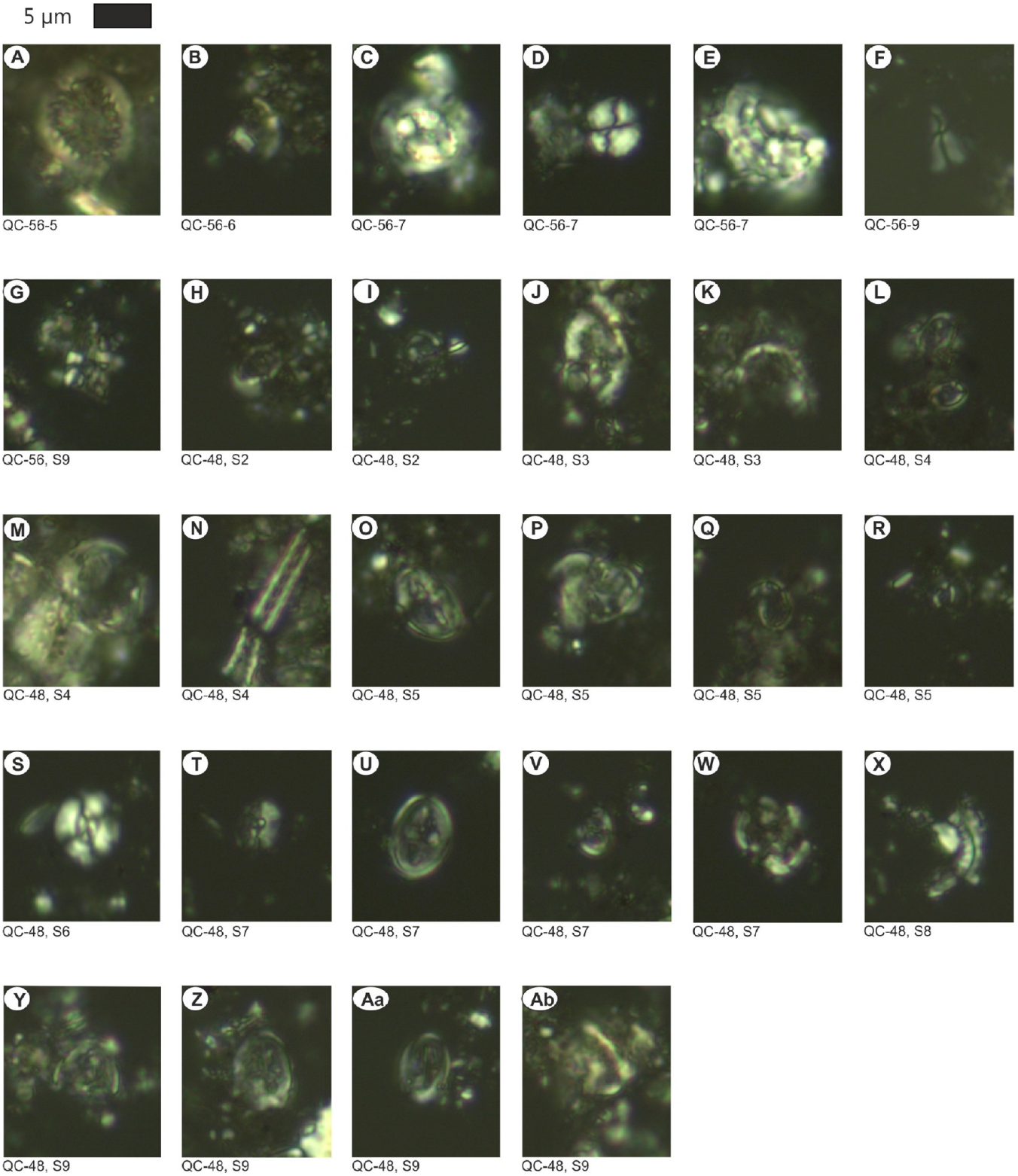

Figure 5. Effect of the rock thermal maturation on nannofossil specimens in boreholes QC-46 and QC-56. (A–Ab) Microphotographs of deformed species.

marine palynomorphs. Terrestrial components (e.g., vitrinite and inertinite) were essentially absent from all the screened samples. Based on these initial findings, vitrinite reflectivity was ruled out as a method for assessing the thermal maturity due to the absence of measurable particles.

Following the initial examination, the whole kerogen and 10 μm sieved fractions of 15 samples from boreholes QC-46, QC-48, and QC-56 were analyzed in transmitted and near-UV blue light. The intensities of kerogen fluorescence, using the fluorescence preservation index (FPI) with a scale ranging from 0 to 4, were used to interpret the thermal maturity, with

https://doi.org/10.1021/acsomega.3c06033
ACS Omega 2023, 8, 39830–39846

higher FPI values corresponding to higher fluorescence intensity, which is generally associated with lower maturity levels.

4. RESULTS

4.1. Calcareous Nannofossil Examination. *4.1.1. Biostratigraphy.* Nannofossil assemblages were found in all the samples but in variable abundances (Figure 2). The distribution of the nannofossils in borehole QC-48 is illustrated in Figure 3. Except for one sample each from boreholes QC-48 and QC-56, which were assigned to the early Eocene (based on the presence of the species *Sphenolithus spiniger*), all of the samples were identified as Maastrichtian (based on the last occurrence of *Lithraphidites quadratus* and *Micula murus*, the marker species for the bases of biozones UC20a and UC20b, respectively).

4.1.2. Calcareous Nannofossil Abundance. Nannofossils were most abundant at the bottom of borehole QC-48, with the other samples in that borehole and in QC-46 and QC-56 having lower abundances, in the "few" to "rare" categories. At least one nannofossil specimen was found in every FOV in QC-48 samples S2, S6, and S11. Samples S7−S10 had "very rare" abundances, with less than one specimen per five FOVs or more. In QC-56, only three samples fell into the "few" category (samples S1, S4 and S5), with the remaining ones containing only "rare" nannofossils. Borehole QC-46 had the lowest nannofossil abundances, with only one sample containing one nannofossil specimen per FOV.

4.1.3. Calcareous Nannofossil Preservation. In borehole QC-46, poor preservation of nannofossils is evident, with dissolution of the rims and central areas, overgrowth of the rims, and general breakage of the specimens recorded. Photomicrographs showing the different degrees of resistance of the nannofossils to deformations are given in Figures 4 and 5, with the distribution of the preservation classes for the three boreholes illustrated in Figure 6. The top two samples (S1 and S2) had moderate preservation with mild overgrowth (O1) in some specimens and moderate dissolution (D2) in others (Figure 4A−D). Heavy dissolution (D3) was observed with depth, reaching a maximum in S7 (Figure 4H−J). It should be noted that S7 exhibited very strong dissolution, making it challenging to identify the species because the rims and central-areas of the nannofossils were all totally or partially affected. Dissolution was detected in S3 and S8 but was not as severe as in S7 (Figure 4E,F,K). Overgrowth was evidenced by enlarged rims, as shown in Figure 4G. There was relatively good preservation in the lowermost sample, S10 (Figure 4M).

Poor preservation with extreme dissolution affected the samples at the top of borehole QC-56 (Figure 4N). The preservation showed a gradual change between samples S3 and S6. Mild dissolution and etching were observed in S3 (Figure 4O,P). The degree of dissolution increased in S4 (Figure 4Q−T) and reached a maximum in S7 (Figures 4V−X and 5B−E). Samples S4 and S6 included some examples of overgrowth (Figures 4U and 5A). The samples showed mild effects of preservation, with many specimens being well preserved but some showing mild overgrowth (Figure 5C). Sample S9 was poorly preserved with intensive dissolution (Figure 5F), whereas the lowest sample (S10) had relatively higher abundance and was better preserved.

Among the three boreholes, QC-48 had the best-preserved nannofossils, with relatively well-preserved specimens found in sample S1 at the top of the borehole followed by moderately

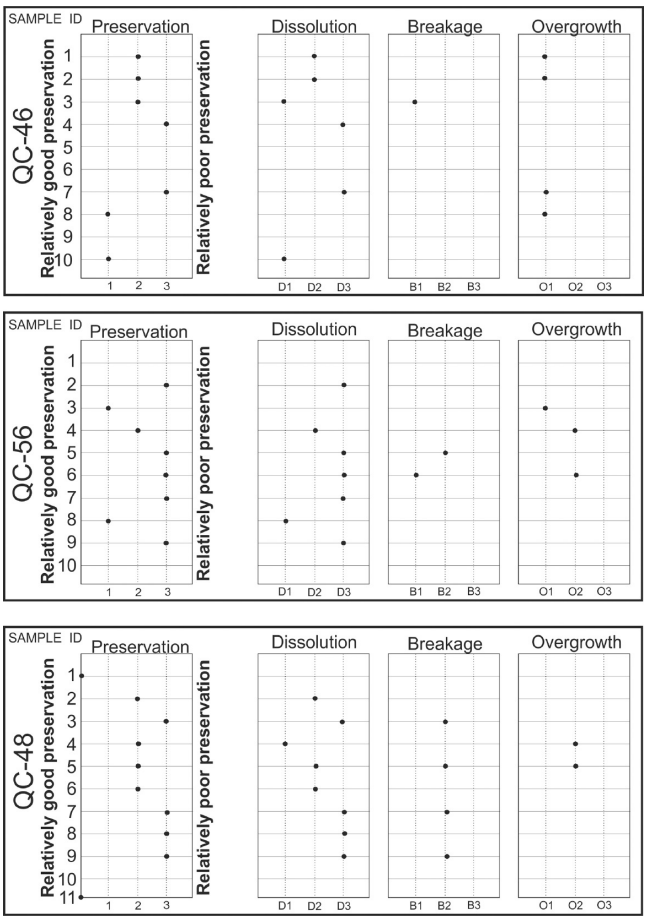

Figure 6. Degree of nannofossil preservation based on summing specimens showing dissolution, breakage, and overgrowth.

preserved nannofossils with dissolution affecting the rims in sample S2 (Figure 5H,I) and then significant dissolution in sample S3 (Figure 5J,K). The deeper samples (S4−S6) had moderate etching due to dissolution and partial overgrowth (Figure 5L−S).

A significant change in preservation was observed in samples S7−S9, which displayed intensive etching and slightly broken nannofossil assemblages (Figure 5T−Ab), in contrast to the relatively well-preserved nannofossils in the lowest samples (S10 and S11).

4.2. Petrographic Examinations. *4.2.1. Kerogen Composition.* The whole-kerogen compositions were recorded as visual estimates of three component groups: liptinite, vitrinite (including nonfluorescent AOM), and inertinite (Table 1). The dominant component of the kerogens was liptinite, with the amount of vitrinite being fairly low and inertinite occurring in trace amounts or being virtually absent. The liptinite was intensely fluorescent AOM yellow and reddish in colors, compared to the vitrinite materials, which were black and nonfluorescent or weakly fluorescent and dull brown AOM. The inertinite was a modified vitrinite, in which the morphologically friable structure had been retained, and it was fluorescent dull brown or black.[45]

Based on these results, the estimated proportion of kerogen components for the borehole samples was separated into six definitive OM categories following Tyson.[46] These categories highlight the dominant kerogen type as well as reveal the organic facies such as fluoramorphinite (FA) − fluorescent

https://doi.org/10.1021/acsomega.3c06033
ACS Omega 2023, 8, 39830−39846

Table 1. Kerogen Composition and Description

borehole	depth (m)	kerogen description	constituents of kerogen					
			FA	HA	AL	HE	WO	CO
QC-46	84.63−84.7	Dominantly moderate brown, strongly cohesive AOM. Rare and poorly preserved marine palynomorphs.	100		Tr			
	85.55−85.6	Dominantly orange brown, low to strongly cohesive AOM. Rare and poorly preserved marine palynomorphs.	100		Tr			Tr
	93.29−93.34	Dominantly orange brown, strongly cohesive AOM. Abundant well preserved marine palynomorphs	95		5			
	95.38−95.49	Moderate brown, low-strongly cohesive AOM. Palynomorphs essentially absent.	100					
	112.86−112.9	Orange brown, strongly cohesive AOM. Palynomorphs absent. Fluorescence is notably weaker than above, likely due to change in preservation.	40	60			Tr	
QC-48	122.29−122.32	Light orange brown, low-moderately cohesive AOM. Rare oil droplets.	100					
	125.39−125.47	Moderately brown, strongly cohesive AOM. Occasional oil droplets	100		Tr			
	140.22−140.25	Dominantly moderate brown, strongly cohesive AOM. Marine palynomorphs very rare.	90	10	Tr		Tr	
	148.64−148.72	Dominantly moderate brown, strongly cohesive AOM. Fairly abundant, poorly preserved, marine palynomorphs.	80	20	Tr			
	151.0−151.06	Dominantly moderate-dark brown, strongly cohesive AOM. Abundant well preserved marine palynomorphs.	90		10			
QC-56	79.7−79.75	Moderate brown, finely disseminated organic matter and moderately cohesive AOM. Organic matter appears darker and possibly more humic than in the deeper samples. Single potential miospore.		100	Tr			
	91.16−91.22	Dominated by orange brown, strongly cohesive AOM. Marine palynomorphs moderately abundant.	90	10	Tr			
	110.67−110.75	Dominated by orange brown, strongly cohesive AOM. Marine palynomorphs moderately abundant.	90	10	Tr			
	113.27−113.31	Dominantly orange brown strongly cohesive AOM. Abundant well preserved marine palynomorphs.	90	5	5			
	136.45−136.52	Mostly orange brown strongly cohesive AOM. Marine palynomorphs common with bacculate orientation.	80	15	5			

AOM, hebamorphinite (HA) − nonfluorescent or weakly fluorescent AOM, algal (AL) OM/phytoplankton − identifiable algae and phytoplankton, including dinocysts, herbaceous (HE) OM-identifiable species and fragments of spores, pollen and leaf cuticles, woody (WO) OM-translucent, structured woody tissues, and coaly (CO) OM-completely opaque, usually angular material.

The FA materials were the dominant constituents of the kerogens, whereas the HE and AL fractions did not exceed 15% and 5%, respectively, in the majority of the samples. This excludes QC-46, sample S10, and QC-56, sample S1, where HE constituted 60% and 100%, respectively, and the OM in both samples appeared darker and more humic than in the other samples. Humic OM is a major indicator of the vitrinite group.[45]

4.2.2. Organic Facies. The organic facies component was investigated using both normal transmitted light and UV light (fluorescence). The dominant kerogen type comprised sapropelic materials (liptinite), which accounted for 85% to 100% in the majority of the samples, with the exception of QC-46, sample S10 (40% sapropelic) and QC-56, sample S1 (0% sapropelic). Based on the palynomacerals, the major organic categories were, in order of abundance, AOM, AL (phytoplankton), HE and zooclasts. An optical examination revealed that the kerogen type was almost entirely made up of AOM, with variable contents of AL, HE, and zooclastic microorganic remnants (Figure 7).

4.2.3. Petrographic Results. Five samples from QC-46 (S1−S10) were analyzed. The AOM was moderate to reddish brown in samples S1 and S7 and orange-brown in samples S3 and S4. Samples S1 and S7 contained light reddish orange fluorescing palynomorphs (FPI 1−2). All petrographic data are listed in Table 1. At the base of the analyzed interval, in S10, the AOM fluorescence was weak brown (FPI 2−3) and no palynomorphs were present. The observed AOM and palynomorph colors and fluorescence suggest equivalent spore color index (SCI) values of 3.0−4.0 for all analyzed samples.

Samples S1−S9 from QC-56 had variable kerogen and palynomorph appearances through the analyzed section. In the shallowest sample analyzed, S1, the kerogen appeared darker and possibly more humic than in the deeper samples, with a single miospore observed with a SCI value of 4.5. The AOM was nonfluorescent in this sample, and the palynomorphs displayed dull brown fluorescence (FPI 3). The AOM in the deeper samples was strongly cohesive and orange in appearance with increasingly stronger fluorescence with depth. In S2, the AOM had brown fluorescence, and the palynomorphs fluoresced yellow-orange and light reddish orange (FPI 2). The palynomorph fluorescence remained yellow-orange and light reddish orange in S5, with the AOM fluorescing light orange brown (FPI 1). In S7, the palynomorphs displayed yellow fluorescence, while the AOM fluorescence was reddish brown (FPI 1). At the base of the analyzed interval (S9), yellow-orange palynomorphs and strong yellow-brown AOM fluorescence were observed (FPI 1). Based on these observations, there appears to be a slight inverse maturity gradient through the section, with equivalent SCI values ranging from 4.0 to 5.0 in S1 to 3.0 to 4.5 in S9.

https://doi.org/10.1021/acsomega.3c06033
ACS Omega 2023, 8, 39830−39846

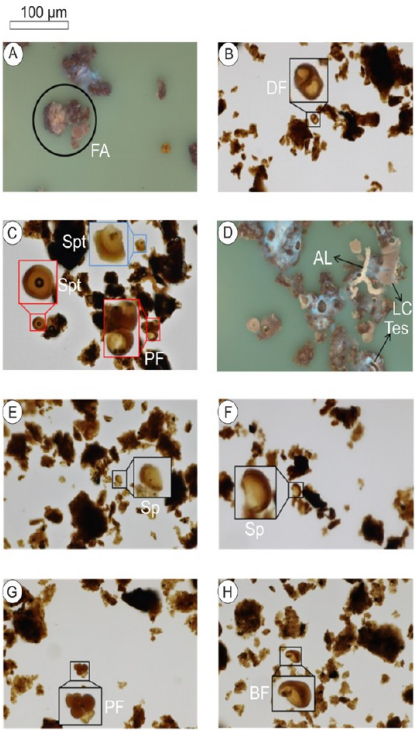

Figure 7. Photomicrographs illustrating types of sieved OM from the shale samples. (A) UV fluorescence structureless, strong brown-yellow AOM with fluoramorphinite (FA). (B) Transmitted light – dorsal view of dinoflagellates. (C) Transmitted light – sporinite (Spt) and planktonic foraminifera (PF). (D) UV fluorescence – alginite (AL), leaf cuticle (LC) and tesmanite (Tes). (E, F) Transmitted light – fragments of spores (Sp). (G) Transmitted light – planktonic foraminifera (PF). (H) Transmitted light – benthic foraminifera (BF). Photomicrographs were taken by A.F.

The kerogens were predominantly composed of fluorescent AOM with minor abundances of algal components in borehole QC-48. Terrestrial components were absent from the majority of samples, with trace amounts of inertinite and vitrinite, probably detrinite, present in samples S3 (85.6 m) and S10 (112.9 m), respectively.

Five samples were analyzed from the QC-48 borehole from 122.32 to 151.06 m (S1–S11). The AOM was light-orange-brown in Sample S1 at the top of the analyzed interval, moderately dark brown between S3 and S9, and dark brown in S11. The fluorescence colors shifted through the analyzed samples, with the AOM in S1 being nonfluorescent (FPI 4) and no recognizable palynomorphs being present. Samples S3 and S6 (140.25 m) contained an orange brown fluorescing AOM and light reddish orange fluorescing palynomorphs (FPI 2). Sample S9 had a stronger orange brown fluorescence, and the palynomorphs displayed a mixture of yellow to yellow orange and light reddish orange fluorescence colors (FPI 1). At the base of the analyzed interval, in S11, the AOM fluoresced reddish brown and the palynomorphs displayed yellow and light reddish orange fluorescence (FPI 3). These observations gave equivalent SCI ranges of 3.5–5.5 in S1 and 3.0–5.0 between S3 and S11.

4.3. Bulk Geochemical Characterization. The percentage by weight of the TOC content varied greatly through the depth profiles of the three cores, ranging from 4.7 to 21.3 wt % (av 15.2 wt %) (Figure 8). Comparably low TOC values (approximately 5 wt %) (Figure 8) were recorded in the two samples from the uppermost parts of QC-48 and QC-56 (samples S1 and S1, respectively). They also had lower pyrolysis parameter (av. S1 = 0.07 mg/g, av. S2 = 1.9 mg/g, and av. S3 = 4.6 mg/g) and HI (avg 34 mg HC/g TOC) values, but a higher OI value (avg 80 mg HC/g TOC).

The pyrolysis data (S1, S2, S3, and T_{max}) are listed in Table 2 and shown in Figures 8 and 9. The samples from QC-48 and QC-56 had similar average values of S1 (~2.3 mg/g), S3 (~1.7 mg/g) and PI ratio (0.03) [defined as S1/(S1 + S2)], whereas higher average values for S2 and lower values for S1, S3, and PI ratio were recorded in QC-46. The S2 values ranged from <1 to 116 mg/g (av. 87 mg/g).

The average HI values were high in all three cores, with maximum values of 706, 633, and 667 mg HC/g TOC for QC-46, QC-48, and QC-56, respectively (Figure 8). The

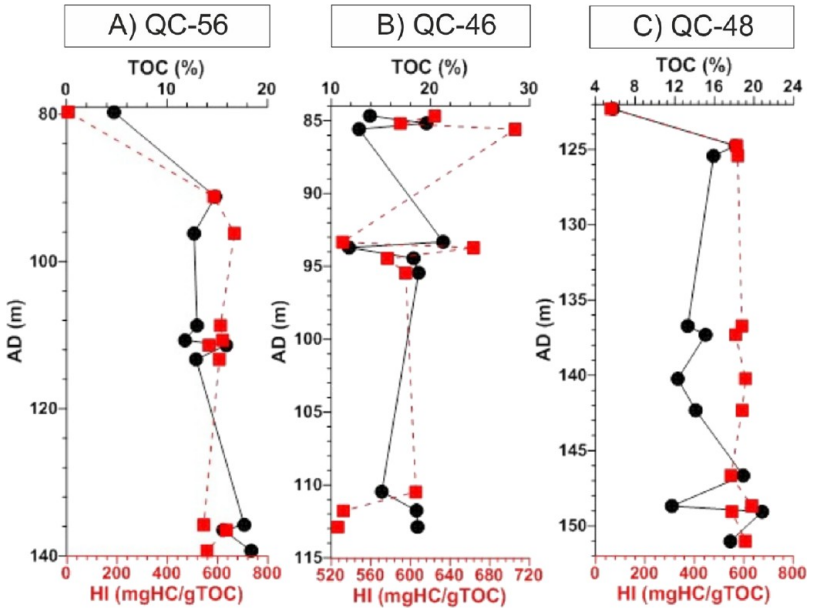

Figure 8. Depth profiles showing variation in the TOC and HI values in (A) QC-56, (B) QC-46, and (C) QC-48.

https://doi.org/10.1021/acsomega.3c06033
ACS Omega 2023, 8, 39830–39846

Table 2. Minimum (min.), Maximum (max.), and Average (av.) Values of the Bulk Geochemical Parameters and Kerogen $\delta^{13}C$ from the Studied Boreholes[a]

Well	Depth Range (m)		TOC (%)	S_1(mg/g)	S_2(mg/g)	S_3(mg/g)	T_{max} (°C)	HI	OI	PI	PP(mg/g)	$\delta^{13}C$‰
QC-56	79.7−139.32	av.	14.8	2.4	87.8	1.3	416.8	599	9	0.03	90.2	−29.1
		max.	18.4	3.1	102.6	1.9	420.0	667	15	0.04	105.1	−28.6
		min.	11.8	1.4	73.2	0.9	414.0	545	7	0.02	75.8	−30.0
QC-46	84.63−112.9	av.	16.9	1.3	99.1	2.8	417.2	595	17	0.01	100.4	−29.4
		max.	21.3	1.9	115.6	3.6	421.0	706	21	0.02	117.2	−28.6
		min.	11.8	0.5	78.3	2.2	413.0	527	11	0.01	79.2	−30.2
QC-48	122.29−151.06	av.	15.8	2.5	91.7	1.4	416.3	584	9	0.03	94.2	−29.1
		max.	20.8	3.6	114.8	1.9	422.0	633	13	0.03	118.4	−28.8
		min.	11.7	1.7	74.0	1.0	412.0	548	7	0.02	75.7	−30.0

[a]TOC = Total organic carbon. S_1-peak = free contents of hydrocarbon(mg HC/g rock); S_2-peak = remaining hydrocarbon potential (mg HC/g rock); S_3 peak = produced carbon dioxide (mg CO_2/g rock); HI = $S_2 \times 100$/TOC (mg HC/g rock); OI = $S_3 \times 100$/TOC (mg CO_2/g TOC); T_{max} = maximum temperature at peak of S_2(°C); PI = production index [$S_1/(S_1 + S_2)$]; PP = petroleum potential ($S_1 + S_2$).

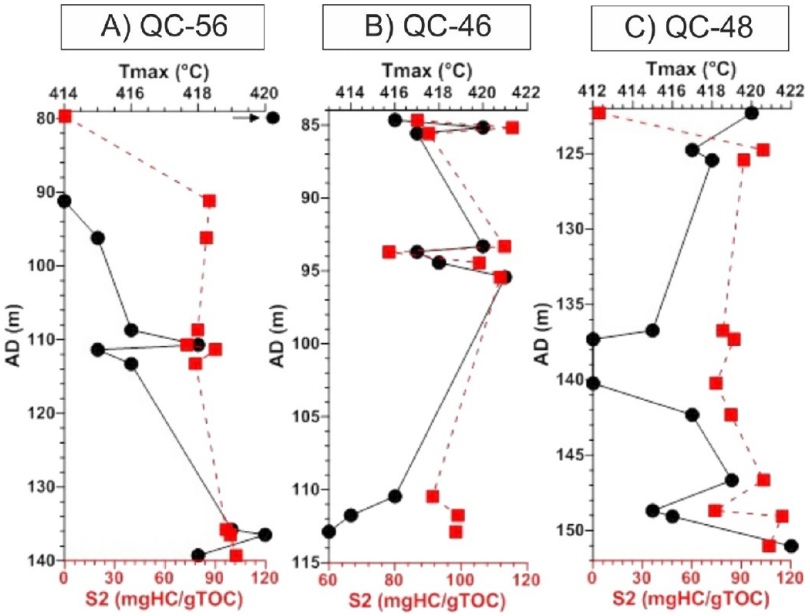

Figure 9. Depth profiles showing variations in T_{max} and S2 values with depth for (A) QC-56, (B) QC-46, and (C) QC-48. Black arrow in panel (A) indicates a sudden increase in T_{max} (to 546 °C) at the top of Borehole QC-56.

corresponding OI had maximum values of 74 and 86 mg of CO_2/g of TOC in QC-48 and QC-56, respectively, with QC-46 having a maximum value of ∼21 mg of CO_2/g of TOC (Table 2).

T_{max}, an indicator of thermal maturation, had similar average values of ∼417 °C among the boreholes, with the highest value being 422 °C in QC-48. The relationship between the T_{max} and depth in QC-46 was highly variable. There was a distinct systematic trend in QC-48, with a gradual decline in the upper part down to sample S5 (∼137 m) and then an overall increasing trend in the lower part, from sample S6 (∼140 m) on down. The trend in QC-56 involved a general increase in T_{max} down to the lowermost samples, from 414 to 420 °C) (Figure 9).

5. DISCUSSION

5.1. Maturity of Organic Matter (OM). The high OM content (expressed as weight percent organic carbon) in the cores varied up to 21.30 wt % (av. 15.2 wt %), with an S2 pyrolysis yield of up to 117 (av. 87) mg HC/g rock and a fairly high average HI of 557 (range <5−706) mg HC/g TOC. Those results suggest excellent HC generative potential, with oil-prone source rocks at peak maturity and a uniform source of OM.

The pyrolysis data and HI versus OI values suggest that all of the samples were predominantly composed of hydrogen-rich Type-IIS kerogen. The low TOC content (∼5%), low average HI value (34 mg HC/g TOC), and higher OI value (av. 80 mg HC/g TOC) suggest the oxidation of OM rather than changes in the OM composition, from predominantly Type-II marine to Type-III terrigenous OM. This oxidation may have been caused by high bioturbation (Figure 1C).

Type-II kerogen is supported by the petrographic analysis, which revealed predominantly oil-prone fluorescent AOM (almost 100% of the total OM, as indicated by common fluorescence). In this case, it was derived largely from marine organisms, with minor abundances of algal components and with no terrestrial contribution.

Due to the absence of terrigenous material, the thermal maturity of the samples was evaluated using Rock-Eval, palynomorph, and AOM color and fluorescence. Because the palynomorphs were marine in nature, exhibiting a wide range of colors not specifically linked to maturity, measuring of the SCI was unsuitable.[47] For this reason, the thermal maturity of

https://doi.org/10.1021/acsomega.3c06033
ACS Omega 2023, 8, 39830−39846

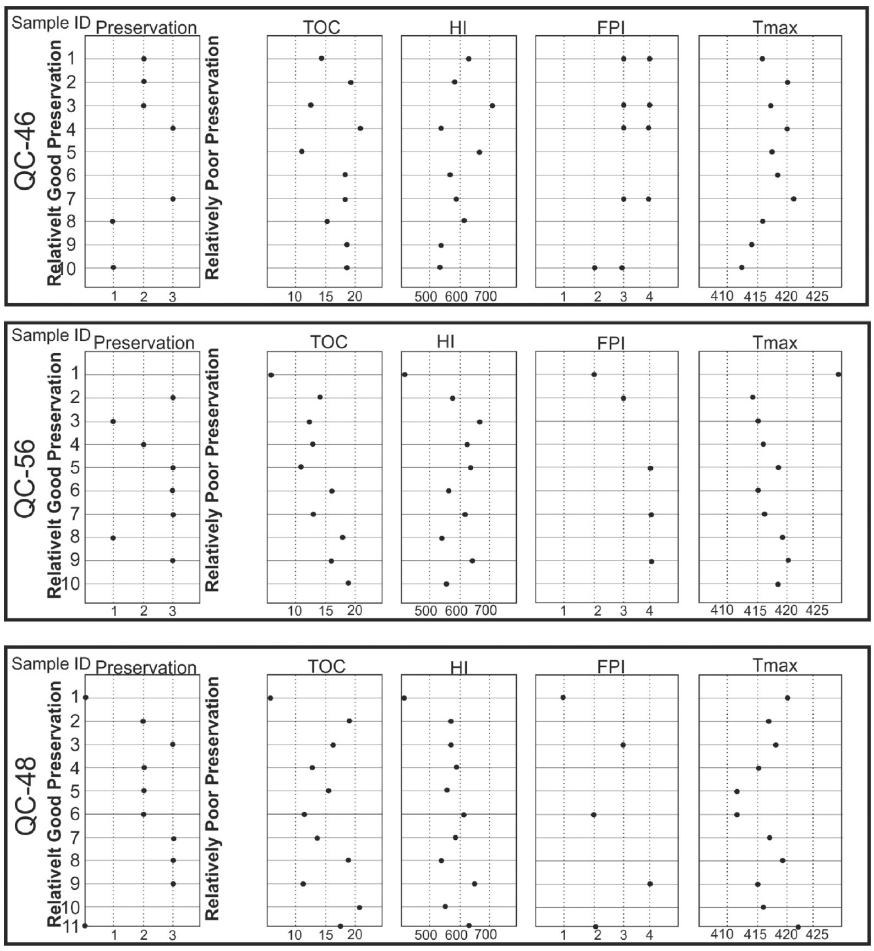

Figure 10. Degree of nannofossil preservation versus TOC, HI, and FPI in the three boreholes.

the samples is expressed as equivalent SCI ranges, based on the above criteria, although it should be noted that the reported palynomorph fluorescence colors are not as sensitive to thermal alteration as those from miospores, where shifts in color can be linked to oil-window maturity. Additionally, preservation appears to have had a significant impact on the appearance of the kerogens, with notable changes in kerogen color and fluorescence across small depth intervals.

The studied MCM Formation samples were part of a larger system of similar facies and age that has been found in many localities, not only in Jordan but also throughout the region.[37,38,48−50] A direct comparison was made with previous work on samples from nearby Upper Cretaceous oil shales of the MCM Formation that had similar TOC enrichment (average ∼10 wt %), HI values (600−700 mg HC/g TOC), and petrographic observations (predominant AOM). This study supports what they found in the similar-age oil shales, but also points to the kerogen being of Type IIS.[48,51,52] Based on bulk kinetic models, the main phase of the HC formation from the thermally immature Upper Cretaceous oil shales of the MCM Formation was determined and occurred between 122 and 148 °C, with a suggested equivalent vitrinite reflectance of between ∼0.56 and 0.65[48] (Hakimi et al. (2018)). This low-temperature generation of HC, due to the lower kinetic energy of cracking S−S compared to C−S bonds, is significantly below the HC threshold for Type-II kerogen (T_{max} >430 °C and corresponding vitrinite reflectance >0.6),[6] but within the range for hydrogen−sulfur-rich Type-II kerogen (T_{max} >410 °C).[53,54] Overall, this finding, concerning the generation of sulfur-rich HCs at an early stage of kerogen cracking, is important for understanding the generation of HCs at relatively shallow burial depths (not exceeding 200m) in the studied cores.

The threshold for oil generation from hydrogen-rich Type-IIS kerogens is 0.39%Ro vitrinite reflectance (∼3.5 SCI),[55] and taking into account the apparent effect of preservation on the optical thermal assessment of the samples, this suggests that the QC-46 samples were largely immature, possibly approaching the oil window at the base, whereas the QC-48 and QC-56 samples were largely in the early oil window.

The optical microscopy results generally correlated with the T_{max} values (412 and 422 °C), indicating overall early oil-window maturity for Type II−S kerogens, considering their lower onset of generation (T_{max} = 410−415 °C) than for normal Type-II kerogen shales.[53,56,57]

5.2. Nannofossil Preservation and FPI Values. A relationship was determined between the nannofossil preservation and FPI (Figure 10). The FPI in QC-46, samples S1 and S7 had values ranging between 1 and 2, which coincided with moderate to poor nannofossil preservation. The FPI value in sample S10 reached 2 to 3, which correlated with better nannofossil preservation. High FPI values in QC-56, samples S2, S5, S7, and S9 correlated well with the nannofossil preservation. However, nannofossils were not present in sample S1 due to metamorphism, which was observed in the field as having affected outcrops in the area. This observation

https://doi.org/10.1021/acsomega.3c06033
ACS Omega 2023, 8, 39830−39846

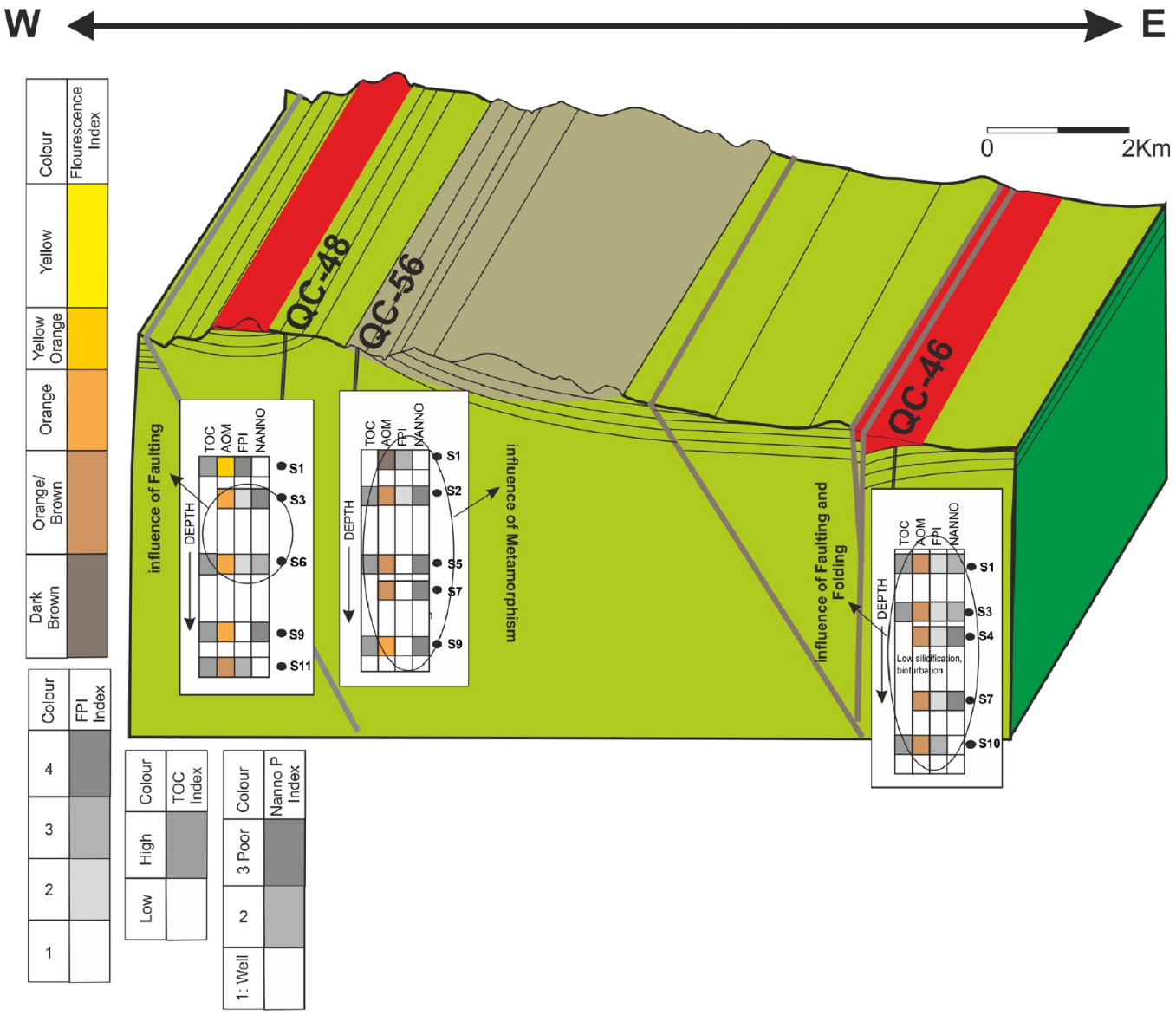

Figure 11. Schematic showing the influence of geological setting on the maturation of organic matter and the preservation of carbonate shells.

was coupled with a high FPI value, further confirming that the uppermost interval had been affected by thermal activity. The topmost and bottommost samples from QC-48 included well-preserved nannofossils associated with higher FPI values. In contrast, lower FPI values were associated with poorly preserved nannofossils in QC-48, samples S3 and S9. The FPI value in sample S6 was consistent with moderate nannofossil preservation.

5.3. Calcareous Nannofossil Preservation versus TOC, HI, and T_{max}. Clear signs of poor preservation, including dissolution of the rims and central areas, overgrowth of the rims, and breakage of the nannofossil specimens, were recorded in the samples and showed trends that correlated with selected bulk geochemical data (Figure 10).

In QC-46, samples S4 and S7, poorly preserved nannofossils were generally present in the samples with higher TOC contents (>18 wt %), lower HI values, and higher T_{max} (>420 °C) (Figure 10). Samples QC-56, S3, S6, and S8 support this observation, with sample S3 having lower TOC and higher HI values than samples S6 and S8, and being associated with better nannofossil preservation. The poorly preserved nannofossils in QC-48, sample S2, were coupled with a high TOC value. The opposite was observed in samples S4 and S6, which contained moderately preserved nannofossils.

A relationship was found between HI and nannofossil preservation, with the low HI value in QC-46, sample S4 being associated with poor preservation and intense nannofossil dissolution. In QC-46, sample S8, a high HI value was associated with moderately good nannofossil preservation. In QC-56, sample S3, relatively well-preserved nannofossils were associated with a high HI value, whereas the opposite was true in samples S5 and S7, where poorly preserved nannofossils occurred alongside high HI values. These nannofossils likely experienced intensive thermal activity, which caused overgrowth of the rims and thereby the poor preservation category of the nannofossils. In QC-48, samples S2, S3, S5, S7, and S8, there was a clear relationship between poor nannofossil preservation (intense dissolution) and low HI values.

Poorly preserved nannofossils were observed in samples with high T_{max} values, including QC-46, samples S4 and S7, QC-56, samples S5−S7 and S9, and QC-48, samples S3 and S7−S9. In QC-48, samples S1 and S11, this correlation did not apply

https://doi.org/10.1021/acsomega.3c06033
ACS Omega 2023, 8, 39830−39846

because the high T_{max} values were associated with relatively good nannofossil preservation. These two samples experienced high bioturbation, which could explain this discrepancy.

5.4. Geological Setting Influence on Calcareous Nannofossil Preservation and Maturity of Organic Matter. All relationships detected in this study indicate that the geological setting significantly influenced the nannofossil preservation and thus the maturity of the OM. We observe a correlation between the degree of nannofossil preservation in the oil-shale samples and the indices of organic petrographic analysis. Because Alqudah et al.[19] and Self-Trail[56] were able to trace the effect of thermal stresses on nannofossils among different sites across the globe, it may be possible to use nannofossils to indicate the level of maturity in oil-shale samples. The poor preservation and high deformation of nannofossils in QC-48, samples S7−S9 coincided with low FPI values (Figure 10) caused by a network of faults crosscutting the study area and encompassing QC-48 (Figure 11). The top sample studied from this borehole (Sample S1) had relatively good nannofossil preservation and a low FPI value. An unconformable surface was distinguished in QC-48, samples S1 and S2, with S1 containing *Sphenolithus spiniger*, which has a range that spans the Ypresian to the Priabonian (NP14−NP17), making this sample Eocene in age. However, the poor preservation in QC-48, sample S1, as indicated by the appearance of the kerogen and the lack of fluorescence, may suggest that its thermal maturity was comparable to that of the other samples in the core.

Comparing the nannofossil preservation between QC-48, sample S1 and QC-56, sample S1, the poor preservation in the latter is obviously due to thermal activity in the restricted metamorphic zone that occurred near the surface in the middle of the study area (Figure 11). According to several authors, such as Powell[35] and Khoury et al.,[57] this unusual metamorphism occurred in central Jordan due to the combustion of oil shales in a restricted basin. No studies have yet determined the peak temperature for the metamorphosed zone. Overall, samples from this core appear to be slightly more thermally mature than samples from other boreholes.

However, Khoury et al.[57] indicated that this metamorphism was low grade. The oil shale closest to the metamorphism showed a higher maturity than that of the other depths. Moderate preservation was detected in QC-46, where large-scale folding was present (plunging syncline). The samples from QC-46 appeared to have a slightly lower thermal maturity than those from QC-48 and QC-56. Given the sedimentary basin setting (the syncline), the significant inverse shift in the FPI over a relatively short depth interval (∼56 m) was likely the result of the variation of kerogen preservation.

The maturity of the OM represented by the T_{max} values in samples from the upper part of QC-48 was abnormally high but dropped abruptly between samples S1 and S5, in the middle of the section, from 420 to 412 °C, before starting a gradual increase to 422 °C toward sample S11 at the base of the section (Figure 9). This unanticipated finding of greater maturities recorded by T_{max}, possibly approaching the onset of HC generation, was consistent with the optically estimated SCI values (generally ranging between 3.0 and 5.0). The shallow depth of the samples suggests that this variation in the maturity, as indicated by the T_{max} and SCI values, was not due to conventional differences in the geothermal gradient but possibly to a different preservation state or, more likely, the influence of thermal stress.

The suggestion of a heat source is supported by field-work observations (Figure 11). One of the subsidiary NE−SW-trending faults, with a strike of 30°N and a dip of 20°SE, was observed to head toward and occur close to samples from the bottom of the QC-48 section. Thus, the slightly higher maturity value noted in QC-48, sample S11 (T_{max} approaching 422 °C), compared to the lower maturity value in sample S5 (T_{max} 412 °C) in the middle of the interval, can be explained by the lower distance to the source of the heat, likely from the attached fault. The higher maturation recorded in QC-48, sample S1 (T_{max} 420 °C) at the top of the core (Figure 9) is most likely attributable to the plunging syncline observed in the field (close to the location where QC-48 was drilled) (Figure 1). Overall, this estimation of a higher level of maturity was further reflected by the highest average (2.5 mg/g) value of free HCs (in QC-48, sample S1).

Borehole QC-46, at a shallower burial depth but with similar OM composition and richness to the other boreholes, had a thinner expression of the organic-rich MCM Formation. Contrary to the observed trend in Tmax in QC-48, and despite being located in an anticline structure and close to a vertical fault, QC-46 appears to be the least mature, with an estimated SCI range of 3.0−4.0 and with no clear maturity trend exhibited by T_{max}.

In QC-56, a maturity-related trend with depth was indicated by a gradual increase in the T_{max}, suggesting no influence of structural features. However, the high maturity value (T_{ma}x = 546 °C) in a spot sample at 112 m in the uppermost part of the borehole was somewhat unexpected and may not accurately reflect the maturity level. This might be related to the thick metamorphosed zone that overlies the MCM Formation, the occurrence of reworked material from older strata, or to the higher bioturbation density (e.g., presence of *Zoophycos* and *Chondrites*). This suggestion of an oxygenated interval is supported by the higher OI value (86 mg of CO_2/g of TOC) and lower HI (5 mg of HC/g of TOC) and TOC (4.7 wt %) values.

5.5. Influence of Early Diagenesis Mechanism on Nannofossil Preservation. Self-Trail[56] described the preservation of nannofossils in impact sediments of the Late Eocene Chesapeake Bay Crater in the eastern USA, where calcite overgrowth developed at the tips and around the edges of the rays of specimens of the genus *Discoaster*. Alqudah et al.,[19] in studying the effect of the Waqf As Suwan meteorite impact on Late Cretaceous nannofossil assemblages, found the upper sediments to have been thermally altered by the impact, which caused partial or complete dissolution of the calcareous nannofossils. Overgrowth was also detected on more resistant species, whereas other taxa were dissolved.

The resistance of certain nannofossil taxa to thermal activities is well documented.[17,19,56] When the sediment is subjected to a source of alteration, such as an intense thermal event, *Discoaster* spp. and *Micula* spp. will remain in an assemblage longer than any other taxa, instead experiencing overgrowth. *Micula* spp. were encountered in QC-46, samples S7−S10, and were more resistant over time than the other species, which likely dissolved due to the harsh environment that would have prevailed during the accumulation of OM. The nannofossils in the other samples in QC-46 were very rare, with *Micula* spp. dominating, likely due to its resistance to the thermal alteration.

In relation to the degradation of abundant OM in the sediment during early diagenesis, porewater alkalinity is a

https://doi.org/10.1021/acsomega.3c06033
ACS Omega 2023, 8, 39830−39846

major factor that influences the preservation of nannofossil assemblages. The change in fluid pH is associated with the very beginning of OM maturation as humic acid occurs along with the production of CO_2 and other components, which turn the environment acidic.[55] The resulting solution significantly affects nannofossil assemblages in two ways: dissolution and overgrowth.

Possible fluid circulation in relation to tectonic activity (folding and faulting) could also have been a factor in nannofossil preservation. Fault systems act as a conduit for meteoric water circulation. Meteoric water is always acidic and oxidizing,[55] which increases the chance of calcite dissolution during OM maturation. The same reasoning applies to folding with the associated joints being conduits for fluid circulation.

6. CONCLUSIONS

A total of 31 samples were investigated in order to determine the nannofossil preservation, TOC, Rock-Eval, and organic petrography. The nannofossils suffered intensive dissolution in the middle parts of the cores and moderate to mild dissolution at the bottom and top. The kerogen recovery was very good in all the samples and predominantly comprised fluorescent AOM with minor AL components. The FPI values were low in most of samples, indicating that the oil shale was subjected to thermal stress. Overall, the vast majority of the samples had high TOC enrichment, with 29 samples exceeding values of >10%. Some trends were apparent in comparing the nannofossil preservation with the different geochemical parameters, including poorly preserved nannofossils occurring in samples with higher TOC contents and lower HI values, and poorly preserved nannofossils occurring with low FPI values and high HC maturity. The low FPI values and a higher level of maturity were associated with poor nannofossil preservation, suggesting that nannofossils, coupled with petrographic analysis could be a rapid tool for estimating levels of oil shale maturity. The nature of the tectonism in the area (faulting, metamorphosed zone) enhanced the maturity and significantly affected the nannofossil preservation.

AUTHOR INFORMATION

Corresponding Author

Mohammed Hail Alhakimi − *Geology Departments, Faculty of Applied Science, Taiz University, 6803 Taiz, Yemen;* orcid.org/0000-0002-3320-9690; Email: ibnalhakimi@yahoo.com

Authors

Mohammad Alqudah − *Department of Earth and Environmental Sciences, Yarmouk University, 21163 Irbid, Jordan;* orcid.org/0000-0002-5255-8394

Mohammad Al Alaween − *Department of Earth and Environmental Sciences, Yarmouk University, 21163 Irbid, Jordan; College of Interdisciplinary Studies, Zayed University, Dubai P.O. Box 19282, United Arab Emirates*

Adam Fermor − *Applied Petroleum Technology (U.K.) Ltd., LL32 8FA Wales, United Kingdom*

Ezaldeen Ali − *Ministry of Energy and Mineral Resources, Amman 11814, Jordan*

Thomas Wagner − *Global Research Institute, The Lyell Centre, Heriot Watt University, EH14 4AP Edinburgh, United Kingdom*

Afikah Rahim − *Department of Geotecnics & Transportation, Faculty of Civil Engineering, Universiti Teknologi Malaysia, 81310 Johor Bahru, Malaysia*

Complete contact information is available at: https://pubs.acs.org/10.1021/acsomega.3c06033

Notes

The authors declare no competing financial interest.

ACKNOWLEDGMENTS

This research was funded by the Dean of Research and Graduate Studies, Yarmouk University (Project No. 05/2019), for which we are grateful. The authors would like to thank two anonymous reviewers for their critical and fruitful comments, which greatly strengthened the manuscript. All material used in this study belongs to Alqamar Co. and permit to publish has been obtained from the company.

REFERENCES

(1) Peters, K.; Cassa, M. R. Applied source rock geochemistry. In *The petroleum System: from Source rock to trap*; Magoon, L. B.; Dow, W. G., Eds; AAPG Memoir 60: 1994; 93−120.

(2) Meyers, P. A.; Doose, H. Sources, preservation, and thermal maturity of organic matter in Pliocene−Pleistocene organic-carbon−rich sediments of the Western Mediterranean Sea. In *1999 Proceedings of the Ocean Drilling Program, Scientific Results*; Zahn, R.; Comas, M. C.; Klaus, A., Eds.; 1999; Vol. *161*: 383−390.

(3) Incarbona, A.; Di Stefano, E. Calcareous nannofossil paleoenvironmental constriction and preservation in sapropel S1 at the Eratosthenes Sea Mount (Eastern Mediterranean). Deep Sea Research II: Topical Studies. *Oceanography* **2019**, *164*, 206.

(4) Parandavar, M.; Sadouni, J. Evaluation of Organic Matter Richness of Eocene Strata Based on Calcareous Nannofossils and Rock-Eval Analysis in North Dezful, Iran. *J. Earth Sci.* **2021**, *32*, 1022−1034.

(5) Espitalie, J. Source Rock Characterization Method for Petroleum Exploration. *Offshore Technology Conference*; Offshore Technology Conference, Houston, TX: 1977; 6.

(6) Peters, K. E. Guidelines for Evaluating Petroleum Source Rock Using Programmed Pyrolysis1. *AAPG Bull.* **1986**, *70* (3), 318−329.

(7) Baskin, D. K. Atomic H/C ratio of kerogen as an estimate of thermal maturity and organic matter conversion. *Am. Assoc. Pet. Geol. Bull.* **1997**, *81* (9), 1437−1450.

(8) Bostick, N. H. Microscopic Measurement of the Level of Catagenesis of Solid Organic Matter in Sedimentary Rocks to Aid Exploration for Petroleum and to Determine Former Burial Temperatures—A Review. *Aspects of Diagenesis*; Scholle, P. A.; Schluger, P. R., Eds.; SEPM Society for Sedimentary Geology, 1979; *26*: 0.

(9) Senftle, J. T.; Landis, C. R. Vitrinite Reflectance as a Tool to Assess Thermal Maturity. *Source and migration processes and evaluation techniques*; Merrill, R. K., Ed.; American Association of Petroleum Geologists, 1991.

(10) Qadri, S. M. T.; Islam, M. A.; Shalaby, M. R.; Ali, S. H. Integration of 1D and 3D modeling schemes to establish the Farewell Formation as a self-sourced reservoir in Kupe Field, Taranaki Basin, New Zealand. *Front. Earth Sci.* **2021**, *15*, 631−648.

(11) Seifert, W. K.; Moldowan, J. M. ″The effect of thermal stress on source-rock quality as measured by hopane stereochemistry. *Phys. Chem. Earth* **1980**, *12* (C), 229−237.

(12) Mackenzie, A. S. *Applications of biological markers in petroleum geochemistry*; 1984.

(13) Carvajal-Ortiz, H.; Gentzis, T. Critical considerations when assessing hydrocarbon plays using Rock-Eval pyrolysis and organic petrology data: Data quality revisited. *Int. J. Coal Geol.* **2015**, *152*, 113−122.

(14) Qadri, S. M. T.; Ahmed, W.; Haque, A. K. M. E.; Radwan, A. E.; Hakimi, M. H.; Abdel Aal, A. K. Murree Clay Problems and Water-Based Drilling Mud Optimization: A Case Study from the Kohat Basin in Northwestern Pakistan. *Energies* **2022**, *15*, 3424.
(15) Horsfield, B.; Douglas, A. G. The influence of minerals on the pyrolysis of kerogens. *Geochim. Cosmochim. Acta* **1980**, *44* (8), 1119−1131.
(16) Nunes, A. A., Abbott, D. H., Glatz, C. A. Microfossil melting by the Ewing impact. 2002; Abstract, abstract volume, Denver annual meeting, session no. 239, paper no. 239−1.
(17) Self-Trail, J. M.; Edwards, L. E.; Litwin, R. J. Paleontological interpretations of crater processes and infilling of synimpact sediments from Chesapeake Bay impact structure. In *The ICDP-USGS deep drilling project in the Chesapeake Bay impact structure: results from Eyreville core holes*; Gohn, G. S.; Koeberl, C.; Miler, K. G.; Reimold, W. U., Eds.; Geological Society of America, special paper 458, 2009; pp 633− 654.
(18) Al-Hejoj, I. K.; Salameh, E.; Abu Hamad, A. Deformed fossils and related structures in Jordan. *Jordan J. Earth Environ. Sci.* **2013**, *5* (1), 31−44.
(19) Alqudah, M.; Khoury, H.; Salameh, E.; Mutterlose, J. A story told by calcareous nannofossils - the timing and course of an Eocene meteorite impact in central Jordan. *Arabian J. Geosci.* **2018**, *11* (16), 451−465.
(20) Armstrong, H.; Braiser, M. *Microfossils*; 2nd ed.; Blackwell Publishing, 2005; 206 pp.
(21) Bender, F. *Geology of the Arabian Peninsula-Jordan*; United States Geological Survey Professional Paper 560-I: WA, 1975; 36 p.
(22) Ziegler, M. Late Permian to Holocene paleofacies evolution of the Arabian Plate and its hydrocarbon occurrences. *GeoArabia* **2001**, *6* (3), 445−504.
(23) Powell, J.; Moh'd, B. Evolution of Cretaceous to Eocene alluvial and carbonate platform sequences in central and south Jordan. *GeoArabia* **2011**, *16* (4), 29−82.
(24) Alsharhan, A.; Nairn, A. *Sedimentary basins and petroleum geology of the Middle East*; Elsevier Science B.V.: Amsterdam, 1997; 843 pp.
(25) Yassini, I. Maastrichtian-Lower Eocene biostratigraphy and the planktonic foraminiferal biozonation in Jordan. *Rev. Esp. Micropaleontol.* **1979**, *11*, 5−57.
(26) Smadi, A. Cretaceous-Paleogene Biostratigraphy Successions in Jordan. *Dirasat, Pure Sci.* **2003**, *30* (2), 262−282.
(27) Abd El-Motaal, E.; Kusky, T. Tectonic evolution of the intraplate s-shaped Syrian Arc Fold-Thrust Belt of the Middle East region in the context of plate tectonics. *Third Int. Conf. Geol. Afr.* **2003**, *2*, 139−157.
(28) Abu-Jaber, N.; Kimberly, M.; Cavaroc, V. Mesozoic-Palaeogene basin development within the eastern Mediterranean borderland. *J. Pet. Geol.* **1989**, *12* (4), 419−436.
(29) Ali Hussein, M. A.; Alqudah, M.; Podlaha, O. G.; van den Boorn, S.; Kolonic, S.; Mutterlose, J. Ichnofabrics of Eocene oil shales from central Jordan and their use for paleoenvironmental reconstructions. *GeoArabia* **2014**, *19*, 145−160.
(30) Alqudah, M.; Ali Hussein, M.; Van den Boorn, S.; Podlaha, O. G.; Mutterlose, J. Calcareous nannofossil biostratigraphy of Eocene oil shales from central Jordan. *GeoArabia* **2014**, *19* (1), 117−140.
(31) Alqudah, M.; Ali Hussein, M.; Podlaha, O. G.; van den Boorn, S.; Mutterlose, J. Biostratigraphy and depositional setting of Maastrichtian−Eocene oil shales from Jordan. *Mar. Pet. Geol.* **2015**, *60*, 87−104.
(32) Abu Qudaira, M. *The Geology of the Wadi Attarat Umm Ghudran*; Natural Resources Authority: Amman, Jordan, 1996.
(33) Diabat, A.; Masri, A. Structural Framework of Central Jordan-Geothermal Project of Central Jordan. *Geol. Mapping Div., Geol. Directorate*; Natural Resources Authority: Amman, Int. Report. 2002.
(34) Bender, F. Geology of Jordan. *The contribution of the Regional Geology of the Earth*; Borntraeger: Berlin, 1974; 196 pp.
(35) Powell, J. H., Stratigraphy and Sedimentation of the Phanerozoic Rocks in Central and South Jordan. *Part B: Kurnub, Ajlun and Belqa Groups, Geological Mapping Bulletin No. 11*; Natural Resources Authority, Amman, 1989; pp 130.
(36) Ali Hussein, M. A.; Alqudah, M.; Blessenohl, M.; Podlaha, O. G.; Mutterlose, J. Depositional environment of Late Cretaceous to Eocene organic rich marls from Jordan. *GeoArabia* **2015**, *20*, 191−200.
(37) Hakimi, M. H.; Abdullah, W. H.; Alqudah, M.; Makeen, Y. M.; Mustapha, K. A. Reducing marine and warm climate conditions during the Late Cretaceous, and their influence on organic matter enrichment in the oil shale deposits of North Jordan. *Int. J. Coal Geol.* **2016**, *165*, 173−189.
(38) Hakimi, M. H.; Abdullah, W. H.; Alqudah, M.; Makeen, Y.; Mustapha, K. A. Organic geochemical and petrographic characteristics of the oil shales in the Lajjun area, Central Jordan: Origin of organic matter input and preservation conditions. *Fuel* **2016**, *181*, 34−45.
(39) Aqleh, S.; van den Boorn, S.; Podlaha, O. G.; Marz, C.; Wagner, T.; Poulton, S.; Kolonic, S. Reconstruction of redox conditions during deposition of Jordan oil shale using inorganic geochemical records. *Mineral. Mag.* **2013**, *77* (5), 603.
(40) Khoury, H.; Nassir, S. High temperature mineralization in Maqarin area, Jordan. *Neues Jahrb. Mineral., Abh.* **1982**, *144*, 197−213.
(41) Perch-Nielsen, K. Mesozoic calcareous nannofossils. In *Plankton stratigraphy*; Bolli, H. M.; Saunders, J. B.; Perch-Nielsen, K., Eds.; Cambridge University Press: Cambridge, 1985; pp 427−554.
(42) Burnett, J. Upper cretaceous. In *Calcareos Nannofossils Biostratigraphy*; Bown, P., Ed.; Chapman and Hall: London, 1998; pp 132−199.
(43) Martini, E. Standard Paleogene calcareous nannoplankton zonation. *Nature* **1970**, *226*, 560−561.
(44) Roth, P. H. Preservation of calcareous nannofossils and fine-grained carbonate particles in mid-cretaceous sediments from the southern Angola Basin, site 530. In *Initial reports of the deep sea drilling project 75*; Hay, W. W.; Sibuet, J.-C., Eds.; 1984; pp 651−655.
(45) Killops, S.; Killops, V.; Killops, S. D.; Killops, V. J. *Introduction to organic geochemistry*; 2 ed.; Blackwell, 2005; 406 pp.
(46) Tyson, R. V. *Sedimentary Organic Matter: Organic Facies and Palynofacies*; Chapman & Hall, London, 1995.
(47) Collins, M. J.; Muyzer, G.; Westbroek, P.; Curry, G. B.; Sandberg, P. A.; Xu, S. J.; Quinn, R.; Mackinnon, D. Preservation of fossil biopolymeric structures: conclusive immunological evidence. *Geochim. Cosmochim. Acta* **1991**, *55* (8), 2253−2257.
(48) Hakimi, M. H.; Abdullah, W. H.; Alqudah, M.; Makeen, Y.; Mustapha, K. A.; Hatem, B. A. Pyrolysis analyses and bulk kinetic models of the Late Cretaceous oil shales in Jordan and their implications for early mature sulpher-rich oil generation potential. *Mar. Pet. Geol.* **2018**, *91*, 764−775.
(49) Hakimi, M. H.; Gharib, A.F.; Alqudah, M.; Ahmed, A.; Hatem, B. A.; Mustapha, K. A.; Abidin, N. S. Z.; Lashin, A.; Yelwa, N. A.; Alqubalee, A. M. Geochemistry and organofacies characteristics of organic-rich chalky marl deposits, northern Jordan: Insights into Type II-S source rock. *J. Asian Earth Sci.* **2022**, *225*, No. 105040.
(50) Hakimi, M. H.; Alqudah, M.; Mustapha, K. A.; Varfolomeev, M. A.; Lashin, A.; Hatem, B. A.; Sen, S.; Radwan, A. E.; Yelwa, N. A. Early-Oil Generation Potential of Type II-S Kerogen in the Upper Cretaceous (Cenomanian−Turonian) Organic-Rich Carbonate Succession from Ajloun Region in Northern Jordan. *Arabian J. Sci. Eng.* **2023**, *48*, 695−710.
(51) März, C.; Wagner, T.; Aqleh, S.; Al-Alaween, M.; Van Den Boorn, S.; Podlaha, O. G.; Kolonic, S.; Poulton, S. W.; Schnetger, B.; Brumsack, H.-J. Repeated enrichment of trace metals and organic carbon on an Eocene high-energy shelf caused by anoxia and reworking. *Geology* **2016**, *44*, 1011−1014.
(52) Qadri, S. M. T.; Shalaby, M.; Islam Hoon, L.L. Source rock characterization and hydrocarbon generation modeling of the Middle to Late Eocene Mangahewa Formation in Taranaki Basin, New Zealand. *Arab J. Geosci.* **2016**, *9*, 559.
(53) Baskin, D. K.; Peters, K. E. Early generation characteristics of a sulfur-rich Monterey kerogen. *AAPG Bull.* **1992**, 1−13.

https://doi.org/10.1021/acsomega.3c06033
ACS Omega 2023, 8, 39830−39846

(54) Lewan, M. D. Oil-generation kinetics for organic facies with Type-II and -IIS kerogen in the Menilite Shales of the Polish Carpathians. *Geochim. Cosmochim. Acta* **2006**, *70* (13), 3351−3368.
(55) Selley, R. C.; Sonnenberg, S. A. *Elements of Petroleum Geology*; 3rd ed.; Academic Press: Amsterdam, 2015; 515 pp.
(56) Self-Trail, J. M. Shock-wave-induced fracturing of calcareous nannofossils from the Chesapeake Bay impact crater. *Geology* **2003**, *31* (8), 697−700.
(57) Khoury, H.; Kock, S.; Likhacheva, A.; Seryotkin, Y.; Belogub, E. Ba and Sr mineralization of fossil fish bones from metamorphosed Belqa group sediments, Central Jordan: an integrated methodology. *Arabian J. Geosci.* **2016**, *9*, 461.

https://doi.org/10.1021/acsomega.3c06033
ACS Omega 2023, 8, 39830−39846